Journal of Alloys and Compounds, 194 (1993) 361–371
JALCOM 7221

Amorphization of mixed Ni and Zr powders by mechanical alloying

Osami Haruyama and Nobuo Asahi
Department of Physics, Faculty of Science and Technology, Science University of Tokyo, 2641 Yamazaki, Noda, Chiba 278 (Japan)

(Received December 9, 1991; in final form June 15, 1992)

Abstract

The amorphization of elemental Ni and Zr powders by mechanical alloying was investigated. The effects of the milling conditions, such as the temperature, intensity and milling tool material, were examined. A higher milling temperature enhances the amorphization reaction and a stronger milling intensity results in the formation of intermetallic compounds. The amount of iron impurity during ball milling with steel tools was several times larger than the tungsten carbide (WC) impurity produced using WC tools, even under similar milling conditions, such as the same number of balls and the same weight of sample. The local structure and thermal properties of mechanically alloyed samples were compared in detail with those of liquid quenched samples.

1. Introduction

Amorphous phases in a large number of metal alloys can be prepared by the rapid solidification technique [1]. During amorphization of a metal alloy by this technique, molten alloy is cooled below the crystallization temperature of the amorphous phase at cooling rates of 10^3–10^{11} K s^{-1} to suppress the nucleation and growth of crystalline phases in the supercooled molten alloy. These high cooling rates restrict the use of this technique of amorphization to specific alloy systems.

In recent years, it has been shown that amorphous alloys can also be prepared by solid state reactions [2–11], such as hydrogen dissolution [2, 3], solid state interdiffusion between multilayers of metal elements [4–7] and mechanical alloying (MA) [8–11]. Of these solid state amorphization reactions, MA can produce an amorphous phase over a wide composition range in several alloy systems.

MA is a high-energy ball milling technique for the production of composite metal powders and crystalline and/or amorphous alloyed powders [12]. This method has been employed for the preparation of dispersion-strengthened alloy powders [13]. However, Koch *et al.* [8] showed that MA could also be employed for the preparation of amorphous alloys. Schwarz and Johnson [4] reported that the mechanism of amorphous phase formation by MA is due to a chemical solid state reaction. The solid state reaction is believed to be caused by the formation of a multilayer structure during milling, the asymmetric interdiffusion couple and the negative heat of mixing, which is considered to be the driving force for diffusion. However, Lee *et al.* [14] have recently reported that amorphous Cu–Ta alloys with a positive heat of mixing can be formed by MA of elemental Cu and Ta powders. Thus a more extensive examination is necessary to establish the fundamental principles of amorphization by MA. Many alloy systems have been amorphized by MA: Ni–Nb [8], Ni–Ti [9], Ni–Zr [15], Fe–Zr [7], Hf–Ni [16], Co–Zr [17], etc. The Ni–Zr binary alloy system has been investigated in detail since amorphous alloys can be prepared by MA and rapid solidification over wide composition ranges and their structural and physical properties can be compared. Hellstern and Schultz [10] were the first to examine the amorphous Ni–Zr alloys produced by MA using X-ray diffraction and calorimetry. Since then many workers have reported amorphous phase formation by MA [14, 18–24]. The glass-forming range produced by MA is narrower in the Ni- and Zr-rich regions than that produced by liquid quenching (LQ) [25, 26]. However, amorphous phase formation by MA is possible in the region 70–90 at.% Ni where LQ cannot be used to prepare amorphous material [25, 26]. In addition, the glass-forming range determined experimentally for MA is in good agreement with that expected theoretically [22], based on Miedema's approach [27]. Structural analysis of amorphous powders by X-ray diffraction [28, 29], neutron diffraction [30], extended X-ray absorption fine structure (EXAFS) [31] and anomalous X-ray scattering (AXS) [32] has indicated that the local structures are similar to those of the corresponding samples prepared by LQ. The milling conditions, such as temperature [33], intensity

0925-8388/93/$6.00

[21, 23] and the material of the milling tool [34], have been reported to play an important role in amorphization by MA.

It is the aim of this study to investigate the amorphization process and thermal stability (including structural analysis) of amorphous Ni–Zr alloy powders prepared by MA, and to compare them with Ni–Zr alloys prepared by rapid solidification. In Section 2, the principles of the MA process are discussed. Section 3 summarizes the amorphization process and thermal stability of amorphous alloys prepared by MA and LQ.

2. MA of elemental powders

2.1. Milling process

MA is a powder processing technique using a high-energy ball mill for the production of composite metal powders and crystalline and/or amorphous alloyed powders. In this section, an outline of the amorphization process by MA of mixed elemental powders is given.

High-energy ball milling is normally performed using a planetary ball mill, a shaker ball mill or a vibratory ball mill [9, 10]. As soon as milling is started, the powder particles which are trapped between colliding balls are subjected to compressive impact forces. The powder particles are severely deformed, fractured and cold-welded and the local temperature is increased by the impact forces. In time powder particles with a characteristically lamellar structure are formed. The lamellar structure is increasingly refined during further milling. Furthermore, interdiffusion between the constituent layers of the lamellar structure becomes active as the local temperature of the particles increases and is significantly enhanced by the high dislocation density and supersaturated point defects which are produced by severe deformation. As a result, the amorphous phase nucleates at the interface region between constituent layers, and develops over the whole region of the powder particle. The amorphous powders thus obtained have a grain size distribution ranging from a few micrometres to about 50 μm.

2.2. Underlying principles

For a qualitative explanation of the MA process, the free energy diagram of a binary system with a negative heat of mixing is useful for predicting the products of the solid state amorphization reaction [35, 36]. As mentioned earlier, amorphization by MA proceeds at relatively low temperatures via an interdiffusion reaction. Unless intermetallic crystalline compounds form during this reaction, we can deduce the metastable phase diagram using the free energy curves. Figure 1 shows the free energy curves for the different phases, *i.e.* amorphous alloy, crystalline intermetallic compound and crystalline terminal solid solutions, in a binary A–B alloy. The full curves are the free energies of the amorphous phase, the crystalline terminal solid solutions and the crystalline intermetallic compound (in this case, this phase does not form). The two broken straight lines are the common tangents between the free energies of the crystalline terminal solid solutions and the amorphous phase. The composition regions of the metastable reaction products, such as the single-phase amorphous alloy or two-phase mixtures of the amorphous alloy and the terminal solid solution of the major element, are determined by the four contact points. This qualitative diagram is appropriate for an explanation of the amorphization of mixed Ni and Zr powders.

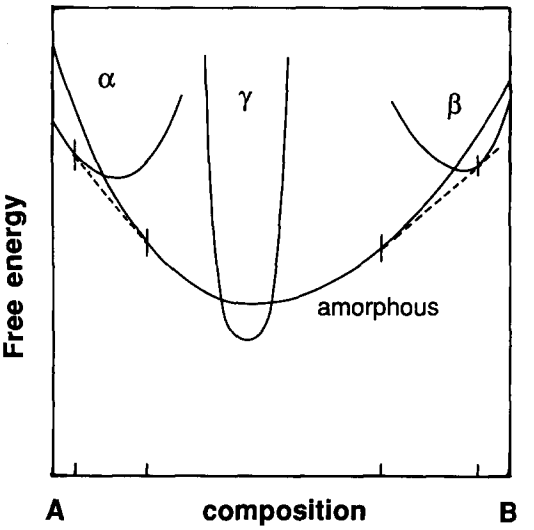

Fig. 1. Free energy diagram for the amorphous phase, intermetallic compound (γ) and terminal solid solutions (α and β).

3. Amorphization and thermal stability of amorphous powders

3.1. X-Ray diffraction and transmission electron microscopy (TEM) observation

The change in the morphology of a composite powder during ball milling can be checked by X-ray diffraction. Figure 2(a) shows X-ray diffraction patterns of $Ni_{80}Zr_{20}$ composite powders milled for 2, 4, 6, 8, 16, 32 and 64 h, using a vibratory mill and tungsten carbide (WC) tools (ball and vessel) [19, 29]. The diffraction peak intensities of Ni and Zr are significantly decreased with increasing milling time. Beyond 16 h all the diffraction peaks of the elemental powders have disappeared and the diffraction peaks of WC (resulting from the debris produced by the collision events between balls and between balls and the wall of the vessel) can be seen. The broad halo pattern typical of the amorphous state gradually appears (after milling of 6 h). The principal

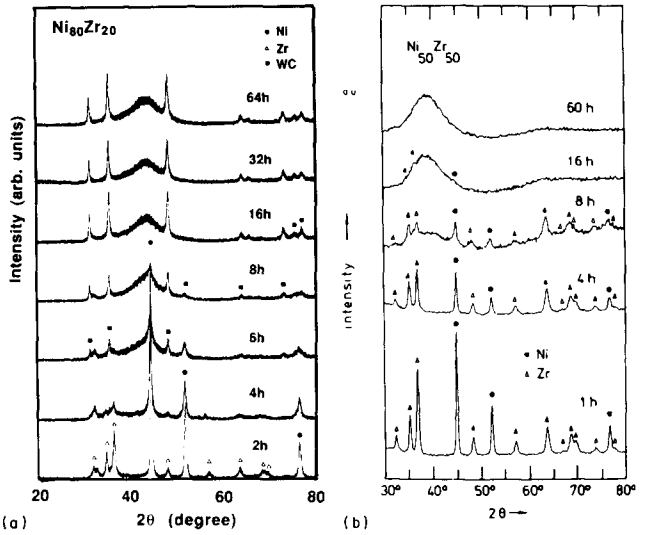

Fig. 2. X-Ray diffraction patterns of mechanically alloyed $Ni_{80}Zr_{20}$ (a) and $Ni_{50}Zr_{50}$ [37] (b) composites subjected to ball milling for different milling times.

peak of the amorphous halo is located between the Ni(111) and Zr(101) diffraction lines. This means that the origin of the halo pattern is not the microcrystallites of the elemental powders produced by ball milling, but the amorphous phase formed by the alloying process based on interdiffusion. No traces of intermetallic compounds were observed in the alloy up to a maximum milling time of 96 h. For comparison, the change in the X-ray patterns of $Ni_{50}Zr_{50}$ composite powders [37], prepared using steel tools, with increasing milling time is shown in Fig. 2(b). The diffraction peak intensities of the elemental powders are gradually reduced with increasing milling time. The fully amorphous state is attained after milling for 60 h. In this case, however, no iron diffraction line is observed during milling.

The texture of the milled powders can be investigated directly by TEM observation. Figure 3 shows the results for $Ni_{50}Zr_{50}$ mechanically alloyed for 8 h [23]. The typical layered microstructure similar to that obtained in other alloy systems [38] can be observed. The amorphous phase grows from the interface region between the elemental Ni and Zr layers. A similar microstructure was observed in the amorphization of an Ni–Zr multilayer produced by vapour deposition and a cold-worked composite wire [39–41]. Therefore, in the initial stage of nucleation of the amorphous phase, both amorphization processes are similar.

Ni(111) and Zr(101) diffraction lines remain visible up to about 8 h of milling. This allows an estimation of the change in the crystallite size of Ni and Zr with increasing milling time. In addition, the interdiffusion of Ni and Zr atoms is presumed from the change in the interplanar spacings with milling time. In Fig. 4, the crystallite size and the interplanar spacing for the

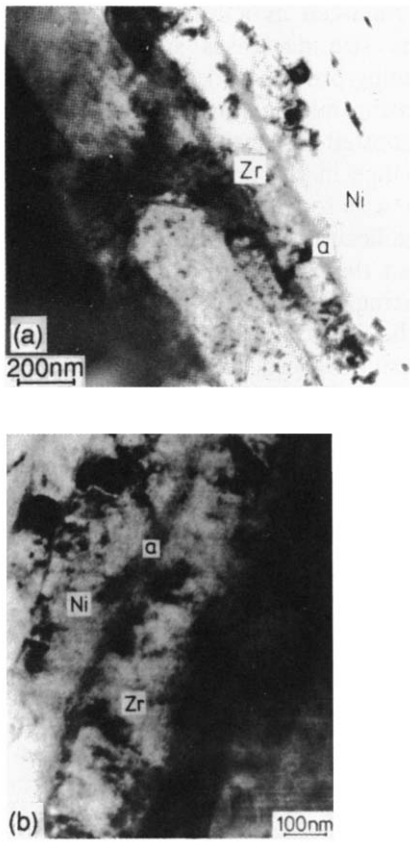

Fig. 3. Transmission electron micrographs of $Ni_{50}Zr_{50}$ [23] composites milled for 8 h; (b) shows detail of (a).

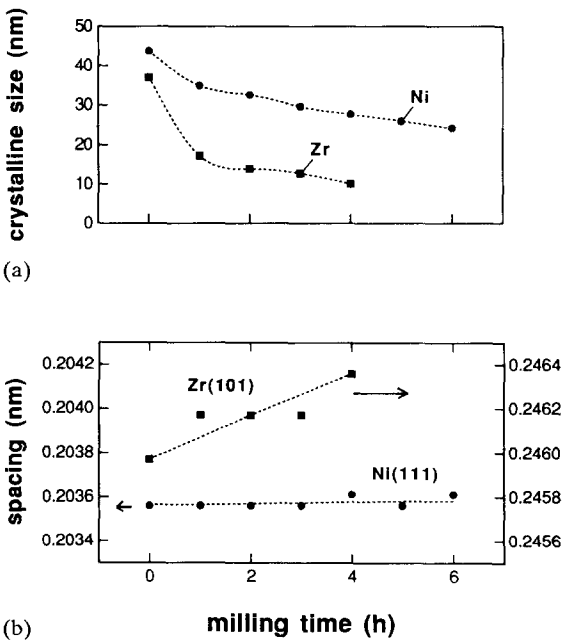

Fig. 4. Ni and Zr crystallite sizes (a) and Ni(111) and Zr(101) interatomic plane spacings (b) for different milling times.

$Ni_{80}Zr_{20}$ alloy are evaluated as a function of milling time. The crystallite size decreases strongly at the beginning of the milling process and is then gradually reduced with increasing milling time. This behaviour is similar to that reported in other alloy systems, *e.g.* Fe–Zr [42]. The change in the crystallite size can be followed for 4 and 6 h for Ni and Zr respectively. Further milling significantly weakens the diffraction peak intensity so that the crystallite size is impossible to estimate. The spacing of the Ni(111) plane increases less than that of the Zr(101) plane with increasing milling time. This result suggests that Ni atoms diffuse primarily into the Zr layer, and agrees with the experimental result [43] that Ni atoms act as the main diffuser in the interdiffusion of the Ni–Zr multilayer.

Figure 5 shows the X-ray diffraction patterns of composite powders after completion of glass formation. The data of Mizutani and Lee [24] in the Ni- and Zr-rich regions show traces of elemental Ni and Zr diffraction lines. It is not clear whether this results from the different milling apparatus (vibratory and planetary). The broad diffuse peak of the amorphous phase shifts to higher diffraction angles with increasing Ni composition. The principal peak position Q_p ($=4\pi \sin\theta/\lambda$) of the halo pattern is known to represent the mean nearest neighbour distance in amorphous alloys [44]. In Fig. 6, the Q_p values of mechanically alloyed samples are compared with those of samples obtained by LQ [26]. The dependence of Q_p on Ni composition is in good agreement for the two techniques. In the composition range $0.7<x<0.9$, where glass formation is difficult by LQ, the Q_p values of mechanically alloyed samples are located on the interpolation line (see Fig. 14, Section 3.5) drawn with the Q_p values at $x=0.7$ and 0.91 in liquid quenched samples.

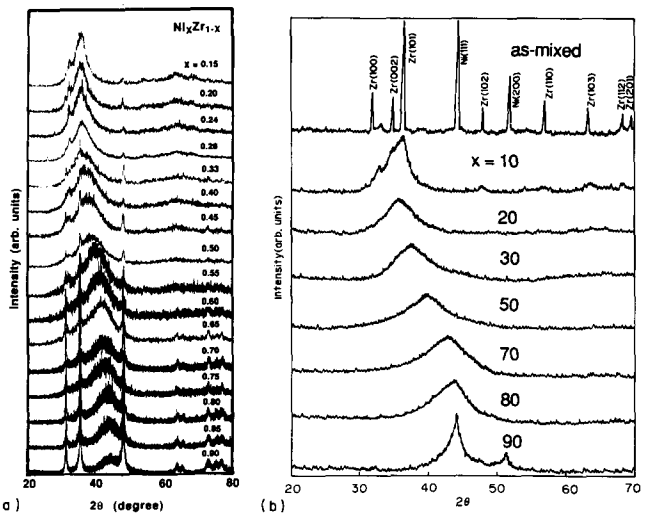

Fig. 5. X-Ray diffraction patterns for Ni_xZr_{1-x} powders milled for 32–64 h (present work) (a) and for 15–20 h [24] (b) with a milling intensity of 9, except for $x=0.7$ (milling intensity, 6).

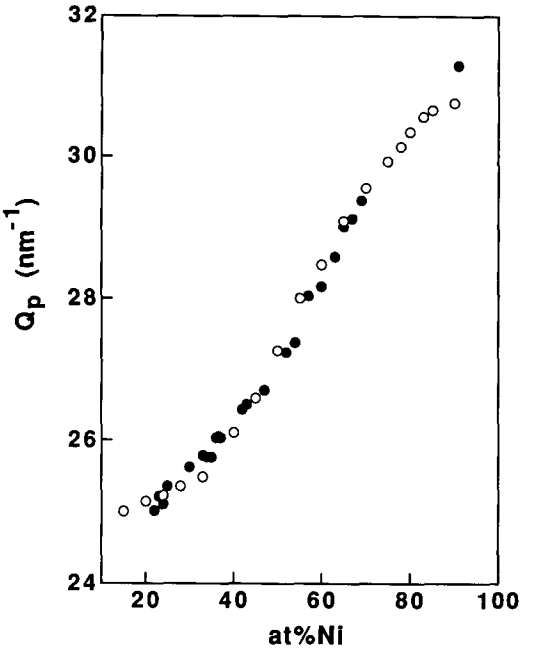

Fig. 6. Wavenumber Q_p of principal halo for Ni_xZr_{1-x} amorphous powders, where ○ and ● correspond to MA (present work) and LQ [26] respectively.

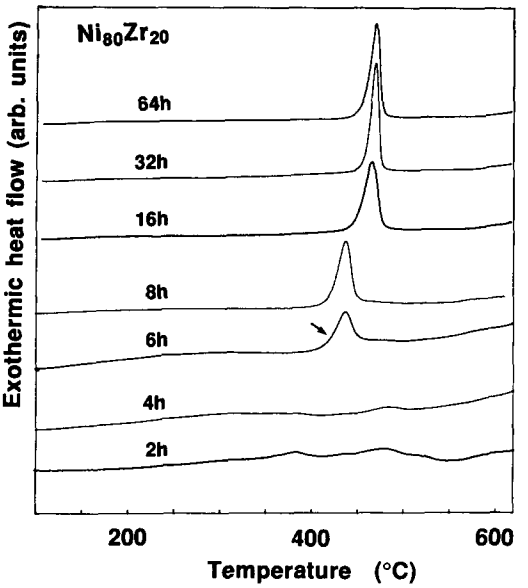

Fig. 7. DSC thermograms of mechanically alloyed $Ni_{80}Zr_{20}$ composites for different milling times (a heating rate of 10 K min^{-1} was used).

3.2. Differential scanning calorimetry (DSC) measurements

The amorphization process was also examined using DSC measurements. Figure 7 shows the change in the DSC thermograms of mechanically alloyed $Ni_{80}Zr_{20}$ composite powders with increasing milling time. The exothermic peak of crystallization (shown by the arrow) of the amorphous phase increases strongly after milling for 6 h. At the beginning of milling (less than 6 h),

a broad exothermic peak is observed in the temperature range 180–380 °C. As no traces of intermetallic compound were detected by X-ray diffraction in the temperature region before the initiation of crystallization, this is considered to result from glass formation and annihilation of defects in unreacted elemental powders due to heating in the DSC apparatus. In Fig. 8, the DSC thermograms of mechanically alloyed samples after completion of glass formation are illustrated, where (a) and (b) correspond to the present work and the results of Eckert *et al.* [21] respectively. Taking into account the difference in the heating rates used (10 K min^{-1} and 40 K min^{-1} for (a) and (b) respectively), there is a good agreement with each other.

3.3. Glass-forming range

The glass-forming range of mechanically alloyed samples has been investigated using physical and thermal properties, such as the superconducting transition temperature [21], saturation magnetization [21, 45], crystallization temperature T_x and crystallization enthalpy ΔH. We consider that the Q_p value of the amorphous halo is also a structurally sensitive property. The Q_p value of liquid quenched samples was used to determine the glass-forming range of mechanically alloyed amorphous powders. The principal halo peak was measured carefully using X-ray diffraction with a step-scanning mode. Figures 9(a) and 9(b) show the Q_p and ΔH values of samples after completion of glass formation as a function of Ni composition in the Ni-rich region. The departure of the Q_p values from the interpolation line, which was drawn using the Q_p values of liquid

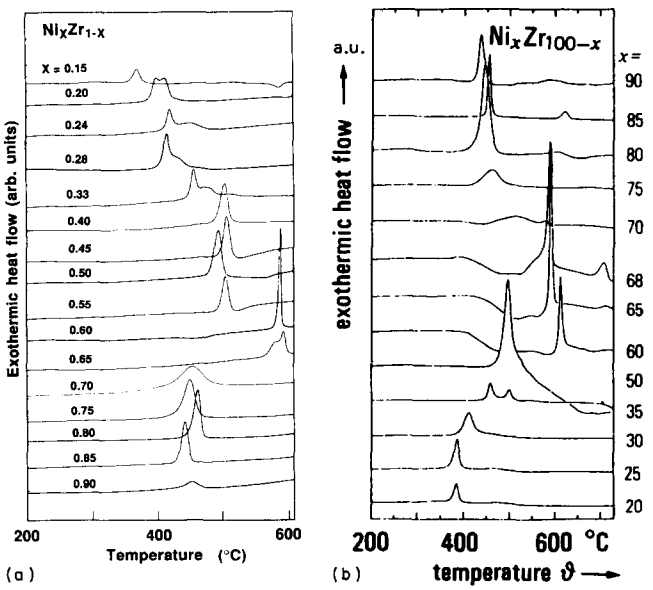

Fig. 8. DSC thermograms of several Ni_xZr_{1-x} samples taken at a heating rate of 10 K min^{-1} (present work) (a) and 40 K min^{-1} [21] (b).

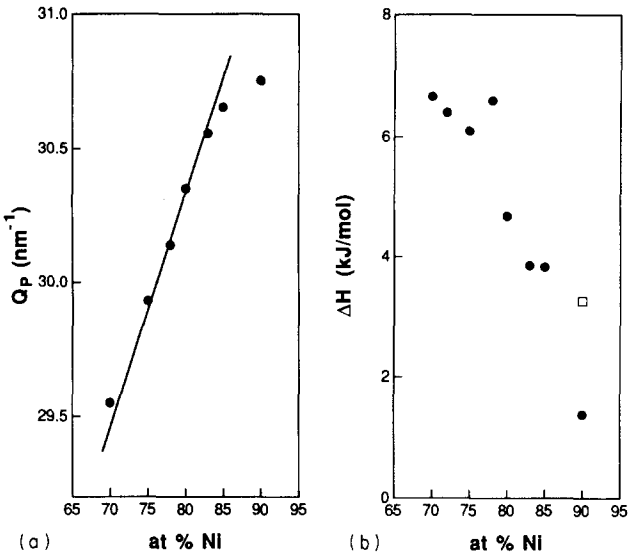

Fig. 9. Q_p (a) and ΔH (b) of mechanically alloyed samples in the Ni-rich region. The ΔH value of the mechanically alloyed sample at $x=0.9$ is fairly small in comparison with the corresponding value [25] of the liquid quenched sample (□). The deviation of the Q_p value from the interpolation line (in Fig. 14, Section 3.5) becomes visible from $x=0.85$.

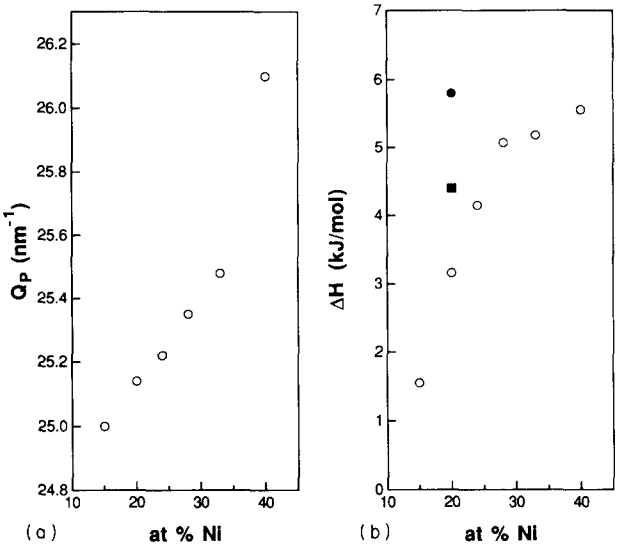

Fig. 10. Q_p (a) and ΔH (b) in the Zr-rich region. The Q_p value decreases homogeneously with decreasing Ni composition. The ΔH value at $x=0.2$ for the mechanically alloyed sample is smaller than that of the liquid quenched sample (●, present; ■, ref. 25).

quenched samples at $x=0.70$ and 0.91, initiates from $x=0.85$. The ΔH value at $x=0.90$ is much lower than that at other compositions and that of the corresponding liquid quenched sample. Consequently, the glass-forming range in the Ni-rich region may be concluded to be less than $x=0.85$. Similar measurements were also carried out in the Zr-rich region and the results are shown in Figs. 10(a) and 10(b). The same discussion is not applicable for the determination of the glass-

forming range in the Zr-rich region, because both ΔH and Q_p decrease homogeneously. In addition, as shown in Fig. 16(a) (see Section 3.6), T_x also exhibits a decrease with increasing Zr composition in the Zr-rich region. However, the T_x values of amorphous powders, prepared using steel tools, saturate as the Zr composition approaches the limitation of glass-forming ability [21]. Therefore it is necessary to examine further the glass-forming ability in the Zr-rich region. Taking into account the observation that the ΔH value of the mechanically alloyed sample is smaller than that of the liquid quenched sample at the composition $x=0.2$, we presume that the glass-forming range is more than $x=0.2$. In Table 1, the glass-forming ranges of mechanically alloyed samples are summarized. For comparison, the glass-forming range of liquid quenched samples [25, 26] and the theoretically expected values [22] based on Miedema's model [27] are given.

3.4. Structural analysis

Structural analysis was used to examine whether the local atomic structure of mechanically alloyed samples is similar to that of liquid quenched samples. Figure 11 shows the radial distribution function (RDF) evaluated from X-ray diffraction data for mechanically alloyed and liquid quenched $Ni_{28}Zr_{72}$, $Ni_{33}Zr_{67}$ and $Ni_{40}Zr_{60}$ alloys [29]. Although some ripples are observed in the data for the mechanically alloyed samples, which may result from the statistical fluctuation of scattered X-radiation, the overall characteristics of the RDF curves of mechanically alloyed samples agree well with those of the liquid quenched samples. The first RDF peak has two distinct subpeaks, corresponding to the atomic Ni–Zr and Zr–Zr correlations; the peak related to the Ni–Ni correlation is invisible due to the small weight ratio W_{NN} multiplied by the Ni–Ni partial RDF for X-ray diffraction. The intensity of the left subpeak increases with increasing Ni composition. The intensity of the right subpeak decreases with increasing Ni composition. The position. This suggests that the left and right subpeaks correspond to atomic Ni–Zr and Zr–Zr correlations respectively. The nearest neighbour distances r_{NiZr} and r_{ZrZr} between Ni and Zr and Zr and Zr atoms, calculated by a curve-fitting procedure with two gaussian functions, are presented in Fig. 12 together with the results

TABLE 1. Glass-forming range of mechanically alloyed samples and liquid quenched samples and the theoretically expected value

Method	Glass-forming range	Apparatus	Tool	Reference
MA	$0.20 \leqslant x \leqslant 0.70$	Not described	Steel	28
	$0.24 \leqslant x \leqslant 0.85$	Shaker	Steel	20
	$0.24 \leqslant x \leqslant 0.83$	Planetary	Steel	21
	$0.20 \leqslant x \leqslant 0.80$	Planetary	Steel	24
	$0.20 < x < 0.85$	Vibratory	WC + steel	Present
LQ	$0.20 \leqslant x \leqslant 0.70$, $x=0.90$			25
	$0.22 \leqslant x \leqslant 0.71$, $x=0.91$			26
Theory	$0.24 \leqslant x \leqslant 0.83$			22

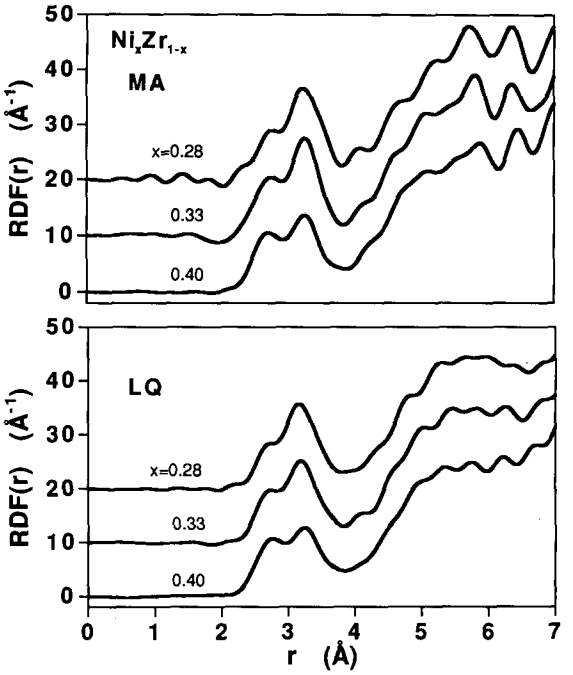

Fig. 11. Radial distribution functions of mechanically alloyed and liquid quenched Ni_xZr_{1-x} ($x=0.28$, 0.33, 0.40) alloys.

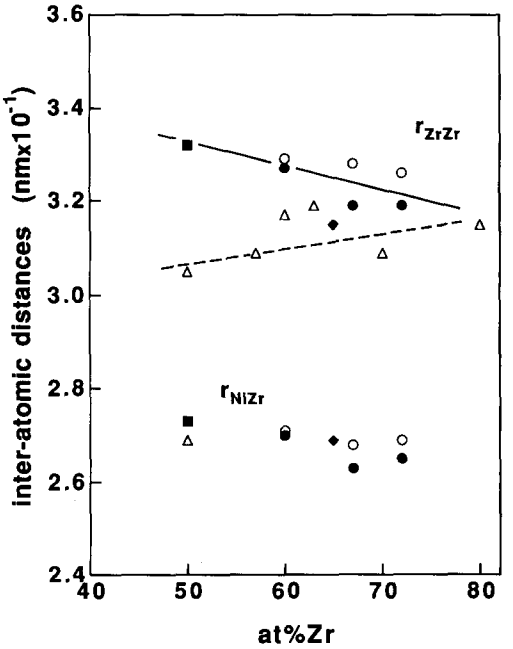

Fig. 12. Nearest neighbour distances r_{NiZr} and r_{ZrZr} obtained from structural analysis for mechanically alloyed (○, present; △, ref. 28) and liquid quenched (●, present; ■, ref. 47; ◆, ref. 46) samples. Full and broken lines are drawn as guides to the eye.

obtained by X-ray [28] and neutron [46, 47] diffraction. The results for mechanically alloyed samples are in good agreement with those of liquid quenched samples. The r_{NiZr} values agree well and decrease slightly with decreasing Ni composition. Our r_{ZrZr} values and the neutron diffraction results agree well and decrease with decreasing Ni composition. However, the r_{ZrZr} values obtained by Burblies and Petzoldt [28] increase with decreasing Ni composition. Both sets of results show a similar tendency in the Zr-rich region (at about $x=0.20$). We believe that this difference in the behaviour of r_{ZrZr} can be attributed to the iron contamination produced from the balls and the vessel during the milling process because, as mentioned later, iron contamination decreases with decreasing Ni composition.

3.5. Effect of milling conditions

The amorphization process is significantly influenced by various milling conditions, such as milling temperature and intensity. Figure 13(a) presents the T_x and ΔH values of $Ni_{33}Zr_{67}$ samples prepared using two milling cycles: mode A, milling for 2 h followed by a rest period to allow the temperature in the vessel to return to room temperature (repeat); mode B, continuous milling for the specified milling time without a rest period. The temperature of the inside wall of the vessel, measured by thermocouples placed in a small hole in the wall, reached 150 °C for mode A and 207 °C after 42 h of milling for mode B. The T_x value for mode B becomes almost constant after 30 h of milling. However, the T_x value for mode A does not saturate even after 42 h of milling. A similar tendency is also observed for ΔH. The X-ray diffraction patterns of $Ni_{50}Zr_{50}$ samples, mechanically alloyed for 15 h at three representative temperatures −120 °C, 25 °C and 200 °C and reported by Lee *et al.* [46], are shown in Fig. 13(b). Glass formation is complete only for milling at 200 °C, where the peak at $2\theta=32.5°$ is attributed to Zr oxide contained in the starting Zr powders. However, the results at other temperatures show the residual diffraction lines of elemental Ni and Zr powders in addition to the broad diffuse halo of the amorphous phase. These results suggest that the diffusion process necessary for amorphization is accelerated by a higher milling temperature.

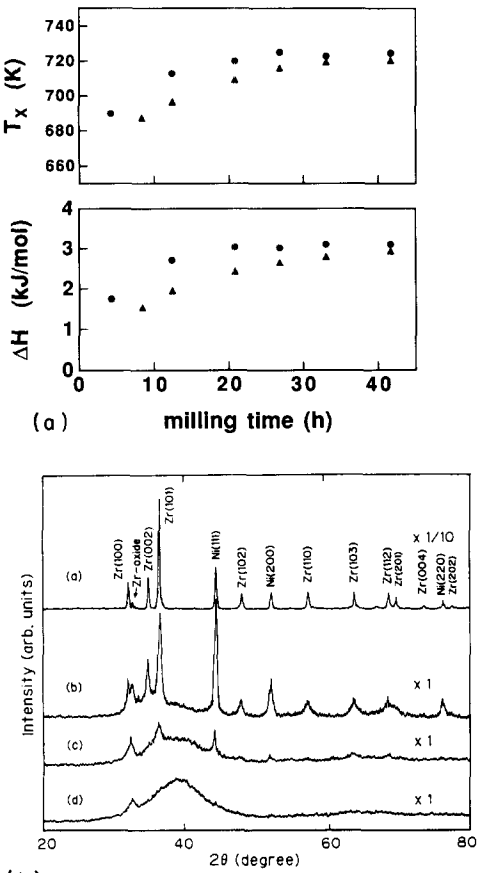

Fig. 13. (a) T_x and ΔH of mechanically alloyed $Ni_{33}Zr_{67}$ composites prepared by two milling cycles (mode A (●) and mode B (▲), see text) for different milling times. (b) The effect of milling temperature T on the X-ray diffraction patterns of $Ni_{50}Zr_{50}$ alloys: (a) as-mixed; (b) $T<-120$ °C; (c) $T=25$ °C; (d) $T=200$ °C [31].

Eckert *et al.* [21] found that the intermetallic compound Ni_3Zr was formed in the composition range $x=0.66$–0.75 using a strong milling intensity ($I=9$) and a planetary-type apparatus. They attributed this to the crystallization induced by the increase in temperature of the powder particles due to the collisions of the balls. Mizutani and Lee [34] investigated in detail the effect of contamination and milling intensity on the amorphization process using a similar planetary-type milling apparatus. They confirmed that the intermetallic compound Ni_3Zr, which is stable and energetically favoured in the phase diagram at this composition, was formed for the $Ni_{70}Zr_{30}$ composite using a high milling intensity ($I=9$). In addition, they confirmed by electron microprobe analysis (EPMA) that the iron contamination for $I=9$ was more than ten times larger than for $I=6$, where Ni_3Zr was not recognized. They concluded that the accumulation of iron and chromium impurities beyond the critical concentration leads to crystallization for $Ni_{70}Zr_{30}$ amorphous powders. It is not known whether the debris from the collision of the balls and vessel dissolves into the amorphous matrix at the atomic level or exists in unreacted micropowders. X-ray diffraction provides the answer. In Fig. 14, the Q_p values of mechanically alloyed and liquid quenched samples are shown in the Ni-rich composition region. The Q_p values of mechanically alloyed samples prepared using steel milling tools are presented together with our results. The Q_p values of samples prepared using steel tools are significantly larger. Since the Q_p values of amorphous materials reflect the change in the mean

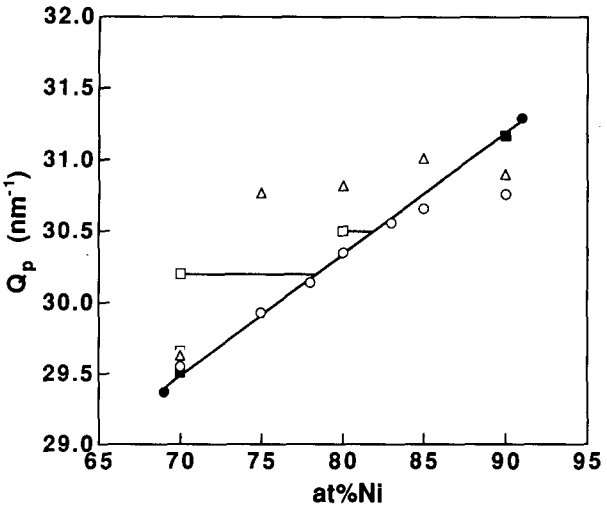

Fig. 14. Q_p values of mechanically alloyed (○, present; □, ref. 24; △, ref. 21) and liquid quenched (●, ref. 26; ■, ref. 24) samples in the Ni-rich region.

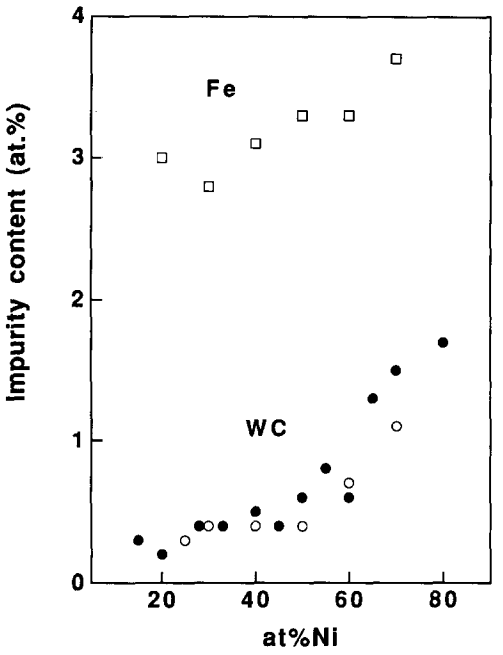

Fig. 15. WC and Fe impurities in samples mechanically alloyed for 32 h with WC (○, ●) and steel (□) milling tools; different ball-to-powder weight ratios (54:1 (○) and 67:1 (●)) were used for ball milling with WC tools.

nearest neighbour distance with alloy composition, this may suggest that the substitution of iron atoms for nickel atoms in the amorphous matrix leads to a decrease in the mean nearest neighbour distance. The r_{ZrZr} value of Burblies and Petzoldt [28] in Fig. 12, produced using steel tools, deviates gradually from the value for liquid quenched and mechanically alloyed samples obtained using WC milling tools as the Ni composition increases. These results indicate that the iron impurities dissolve into the amorphous matrix so that the real Zr composition decreases. Mizutani and Lee [24] have reported that the horizontal shift shown in Fig. 14 corresponds to the iron impurity dissolved into the amorphous matrix. The good agreement between the Q_p values of mechanically alloyed and liquid quenched samples, obtained using WC tools, suggests that the crystalline WC debris produced during milling does not dissolve into the amorphous matrix but remains isolated between composite powders. To confirm this conclusion, microscopic measurements, such as Mössbauer spectroscopy and photoelectron emission spectroscopy, are required.

In order to compare the WC and iron impurity quantitatively, ball milling for 32 h with WC and steel tools was performed under the same milling conditions (ball radii and number, sample weight) [34]. The results obtained are presented in Fig. 15, where different ball-to-powder weight ratios were employed for the preparation process with WC tools. WC and iron contamination increases with increasing Ni composition. The iron contamination is about four times larger than the WC contamination after ball milling for 32 h.

3.6. Thermal stability

Figure 16 shows the dependence of T_x, ΔH and the activation energy E_c of crystallization on Ni composition, where E_c was obtained from rate-dependent measurements using Kissinger's analysis [48]. In Fig. 16(a), our T_x results are illustrated together with the results of liquid quenched samples obtained by Buschow [26]. The overall change in T_x with Ni composition is similar for both sets of results. However, when it is considered that different heating rates were employed, *i.e.* 10 K min^{-1} in our experiment and 50 K min^{-1} in Buschow's measurement, our results in the Zr-rich region show slightly higher T_x values. This may be ascribed to oxide contamination as reported by Brüning *et al.* [49]. The maximum of T_x around $x=0.60$ in liquid quenched samples is well reproduced in mechanically alloyed samples.

The two sharp peaks in Fig. 16(b), which presents the relationship between the E_c value and the Ni composition, occur for both liquid quenched and mechanically alloyed samples at $x=0.38$ and $x=0.65$ which correspond to the two innermost eutectics. However, the E_c values at the maximum positions are smaller for mechanically alloyed samples.

Figure 16(c) shows the behaviour of ΔH in liquid quenched and mechanically alloyed samples. In this case our results for liquid quenched and mechanically alloyed samples are not in satisfactory agreement, in contrast with T_x and E_c. For this reason, other results for liquid quenched samples [25, 26] were used. The peak around $x=0.28$ appearing in Buschow's [26] results is not satisfactorily reproduced in our data or the results of Altounian *et al.* [25]. Although the liquid quenched

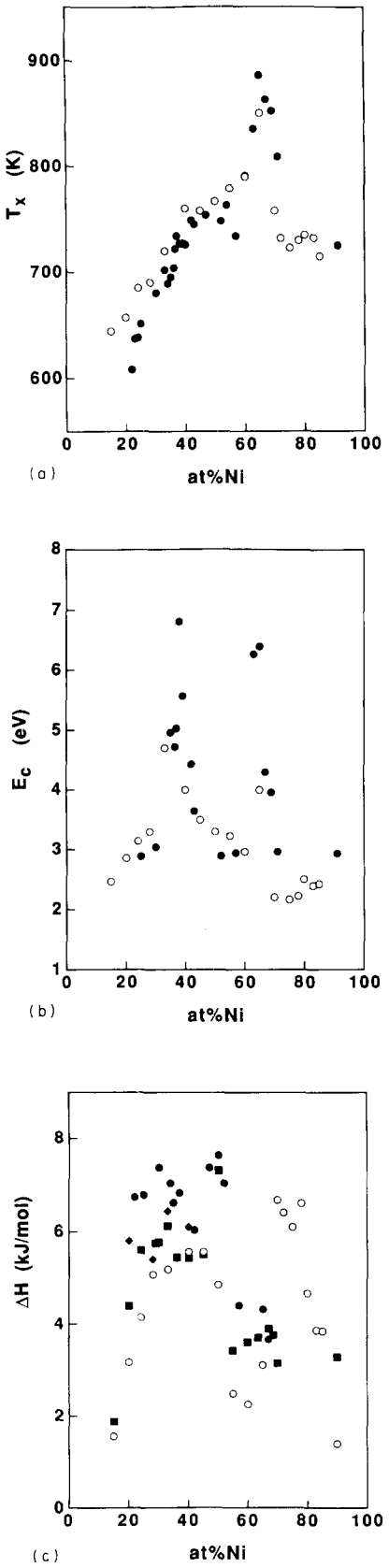

Fig. 16. Composition dependence of the kinetic parameters T_x (a), E_c (b) and ΔH (c) for mechanically alloyed (○) and liquid quenched (◆, present; ●, ref. 26; ■, ref. 25) samples.

samples exhibit a sharp peak around $x=0.5$, this peak is not observed in mechanically alloyed samples, but a broad peak extending from $x=0.20$ to $x=0.50$ is observed. Between $x=0.7$ and $x=0.78$, the mechanically alloyed samples exhibit a broad ΔH peak. Unfortunately, the corresponding liquid quenched samples are not available in this region. However, this result agrees with the theoretical prediction [50] based on ΔH derived from the formation enthalpy of crystalline and amorphous alloys.

Amorphous material with high E_c and low ΔH values is stable thermodynamically, because ΔH is a measure of the driving force for initiation of crystallization and E_c is a measure of the kinetic motion of the atoms. This is satisfied only at the composition $x=0.65$, one of the two innermost eutectics. However, this condition is not sufficiently reproduced around the other eutectic compositions. At $x=0.50$ and $x=0.78$, which correspond to the top of the liquid phase line in the binary phase diagram (existence of the congruently melting compounds NiZr and Ni_7Zr_2), there is a close correlation between high ΔH and low E_c. It is accepted [51] that the deep eutectic is a region of easy glass formation, because the liquid structure is maintained until relatively low temperatures during rapid quenching. However, Buschow [26] has reported that easy glass formation does not necessarily correspond to high thermal stability. This tendency is also applicable to mechanically alloyed amorphous samples. In regions which correspond to the top of the liquidus line, however, glass formation is relatively difficult during liquid quenching. The results obtained show that, in this case, the amorphous phase exhibits low thermal stability. However, it is not clear why this consideration is not applicable to the corresponding composition ($x=0.33$) in the Zr-rich region.

4. Conclusions

The following conclusions can be drawn from this study.

(1) The glass-forming range of mechanically alloyed samples exists within the limits of the glass-forming range for liquid quenched samples. However, MA can be used to produce amorphous material in the composition region 70–90 at.% Ni where liquid quenching is not suitable.

(2) The influence of the milling conditions is very significant. The crystalline intermetallic compound Ni_3Zr is produced frequently during ball milling with high intensity [21, 24]. This can be attributed to the crystallization induced by the increase in local temperature of the particles and the effects of iron and chromium impurities produced during ball milling.

(3) The results of structural analysis indicate the similar local structures for both samples (MA and LQ) in the Zr-rich region. However, the nearest neighbour distance r_{ZrZr} between Zr atoms, obtained by Burblies and Petzoldt [28], exhibits smaller values with increasing Ni content. We presume that this results from a mechanism, as yet unknown, associated with the iron impurity introduced into the amorphous matrix, because the content of iron impurity increases with increasing Ni content.

(4) The kinetic parameters T_x and E_c depend similarly on the Ni composition. However, the ΔH values of mechanically alloyed samples are smaller than those of liquid quenched samples. If we consider that ΔH is a volume-dependent property, this may indicate that microcrystallites of elemental powders remain unreacted even after the completion of amorphization (checked by X-ray diffraction). Further TEM observations may be necessary. However, it is also possible that the chemical short-range order (CSRO) in amorphous materials closely corresponds to ΔH [50].

It is not known why the formation of intermetallic compounds is suppressed while the amorphous phase nucleates. The results of the amorphization process in Ni–Zr multilayers may provide an interesting suggestion. In this system, the nucleation and growth mechanisms of the amorphous phase and the intermetallic Ni–Zr compound have been reported to be competing rate-controlled mechanisms [40]. Following this model, the growth of the amorphous phase stops and the growth rate of the intermetallic compound surmounts that of the amorphous phase due to the reduction in the diffusibility of diffusion couples through the amorphous phase as a result of structural relaxation. In the amorphous phase subjected to MA, this relaxation may not occur. Therefore, the amorphization reaction will continue until the amorphized region covers the particle.

References

1 P. Duwez, R. H. Willens and W. Klement, Jr., *Nature (London), 187* (1960) 869.
2 S. K. Malik and W. E. Wallace, *Solid State Commun., 24* (1977) 283.
3 X. L. Yeh, K. Samwer and W. L. Johnson, *Appl. Phys. Lett., 42* (1983) 242.
4 R. B. Schwarz and W. L. Johnson, *Phys. Rev. Lett., 51* (1983) 415.
5 R. B. Schwarz, K. L. Wong, W. L. Johnson and B. M. Clemens, *J. Non-Cryst. Solids, 61, 62* (1984) 129.
6 M. V. Rossum, M. A. Nicolet and W. L. Johnson, *Phys. Rev. B, 29* (1984) 5498.
7 B. M. Clemens and M. J. Suchoski, *Appl. Phys. Lett., 47* (1985) 943.
8 C. C. Koch, O. B. Cavin, C. G. McKamey and J. O. Scarbrough, *Appl. Phys. Lett., 43* (1983) 1017.
9 R. B. Schwarz, R. R. Petrich and C. K. Saw, *J. Non-Cryst. Solids, 76* (1985) 281.
10 E. Hellstern and L. Schultz, *Appl. Phys. Lett., 48* (1986) 124.
11 C. Politis and W. L. Johnson, *J. Appl. Phys., 60* (1986) 1147.
12 J. S. Benjamin, *Sci. Am., 234* (1976) 40.
13 J. S. Benjamin and M. S. Bamford, *Metall. Trans. A, 8* (1977) 1301.
14 C. H. Lee, M. Mori and U. Mizutani, *J. Non-Cryst. Solids, 117, 118* (1990) 733.
15 B. M. Clemens, W. L. Johnson and R. B. Schwarz, *J. Non-Cryst. Solids, 61, 62* (1984) 817.
16 M. van Rossum, M. A. Nicolet and W. L. Johnson, *Phys. Rev. B, 29* (1984) 5498.
17 H. Schöder, K. Samwer and U. Köster, *Phys. Rev. Lett., 54* (1985) 197.
18 E. Gaffet, N. Merk, G. Martin and J. Bigot, *J. Less-Common Met., 145* (1988) 251.
19 O. Haruyama and N. Asahi, *Proc. Int. Symp. on Mechanical Alloying, Kyoto, Japan, May 1991,* in *Mater. Sci. Forum, 88/89* (1992) 333.
20 P. Y. Lee and C. C. Koch, *J. Mater. Sci., 23* (1988) 2837.
21 J. Eckert, L. Schultz, E. Hellstern and K. Urban, *J. Appl. Phys., 64* (1988) 3224.
22 A. W. Weeber and H. Bakker, *Physica B, 153* (1988) 93.
23 J. Eckert, L. Schultz and K. Urban, *J. Mater. Sci., 26* (1991) 446.
24 U. Mizutani and C. H. Lee, *J. Mater. Sci., 25* (1990) 399.
25 Z. Altounian, G.-H. Tu and J. O. Strom-Olsen, *J. Appl. Phys., 54* (1983) 3111.
26 K. H. J. Buschow, *J. Phys. F, 14* (1984) 593.
27 A. R. Miedema, P. F. de Châtel and F. R. de Boer, *Physica B, 100* (1980) 1.
28 A. Burblies and F. Petzoldt, *J. Non-Cryst. Solids, 107* (1989) 233.
29 O. Haruyama, A. Kuroda and N. Asahi, *Proc. 5th Int. Conf. on Non-Crystalline Materials, Sendai, 1991,* in *J. Non-Cryst. Solids, 150* (1992) 483.
30 K. Suzuki, *J. Non-Cryst. Solids, 112* (1989) 23.
31 F. Itoh, T. Sekiuchi, M. Sakurai, T. Fukunaga and K. Suzuki, *Trans. Jpn. Inst. Met., 29* (1988) 15 (Suppl.).
32 A. Corrias, F. Buffa, G. Licheri, G. Navarra and D. Raoux, *Proc. 5th Int. Conf. on Non-Crystalline Materials, Sendai, 1991,* in *J. Non-Cryst. Solids, 150* (1992) 487.
33 C. H. Lee, M. Mori, T. Fukunaga and U. Mizutani, *Jpn. J. Appl. Phys., 29* (1990) 540.
34 N. Asahi, O. Haruyama and R. Wagner, *J. Alloys Compounds,* to be submitted.
35 W. Hume-Rothery and E. Anderson, *Philos. Mag., 5* (1960) 383.
36 L. Schultz, *Mater. Sci. Eng., 97* (1988) 15.
37 J. Eckert, L. Schultz and K. Urban, *J. Non-Cryst. Solids, 130* (1991) 273.
38 F. Petzoldt, B. Scholz and H. D. Kunze, *Mater. Lett., 5* (1987) 280.
39 R. J. Highmore, R. E. Somekh, A. L. Greer and J. E. Evetts, *Mater. Sci. Eng., 97* (1988) 83.
40 W. J. Meng, C. W. Nieh, E. Ma, B. Fultz and W. L. Johnson, *Mater. Sci. Eng., 97* (1988) 87.
41 L. Schultz, *Z. Phys. Chem. Neue Folge, 157* (1988) 257.
42 L. Schultz, *J. Less-Common Met., 145* (1988) 233.
43 Y. T. Cheng, W. L. Johnson and M. A. Nicolet, *Appl. Phys. Lett., 47* (1985) 800.
44 R. C. Ruhl, B. C. Giessen, M. Cohen and N. J. Grant, *Acta Metall., 15* (1967) 1693.
45 J. Eckert, L. Schultz and K. Urban, *J. Less-Common Met., 166* (1990) 293.

46 A. Lee, G. Etherington and C. N. J. Wagner, *J. Non-Cryst. Solids, 61, 62* (1984) 349.
47 T. Fukunaga, N. Hayashi, N. Watanabe and K. Suzuki, *Proc. 5th Int. Conf. on Rapidly Quenched Metals, Würzburg, 1985,* Vol. 1, North-Holland, Amsterdam, 1985, pp. 483–486.
48 H. E. Kissinger, *Anal. Chem., 29* (1957) 1702.
49 R. Brüning, Z. Altounian, J. O. Strom-Olsen and L. Schultz, *Mater. Sci. Eng., 97* (1988) 317.
50 M. P. Henaff, C. Colinet, A. Pasturel and K. H. J. Buschow, *J. Appl. Phys., 56* (1984) 307.
51 H. A. Davies, *Phys. Chem. Glasses, 17* (1976) 159.